Three decades of intersatellite-calibrated High-Resolution Infrared Radiation Sounder upper tropospheric water vapor

Lei Shi[1] and John J. Bates[1]

Received 29 July 2010; revised 8 December 2010; accepted 28 December 2010; published 22 February 2011.

[1] To generate a climatologically homogenized time series of the upper tropospheric water vapor (UTWV), intersatellite calibration is carried out for 3 decades of High-Resolution Infrared Radiation Sounder (HIRS) channel 12 clear-sky measurements. Because of the independence of the individual satellite's instrument calibration, intersatellite biases exist from satellite to satellite. To minimize the expected intersatellite biases, measurement adjustments are derived from overlapping HIRS data from the equator to the poles to account for the large global temperature observation range. Examination of the intersatellite biases shows that the biases are scene temperature–dependent. Many overlapping satellites have bias variations of more than 0.5 K across the scene temperature ranges. An algorithm is developed to account for the varying biases with respect to brightness temperature. Analyses based on the intercalibrated data show that selected regions of UTWV are highly correlated with low-frequency indexes such as the Pacific Decadal Oscillation index and the Pacific and North America index, especially in the winter months. The derived upper tropospheric humidity in the central Pacific also corresponds well with the Niño 3.4 index. Thirty year trend analysis indicates an increase of upper tropospheric humidity in the equatorial tropics. The areal coverage of both high and low humidity values also increased over time. These features suggest the possibility of enhanced convective activity in the tropics.

Citation: Shi, L., and J. J. Bates (2011), Three decades of intersatellite-calibrated High-Resolution Infrared Radiation Sounder upper tropospheric water vapor, *J. Geophys. Res.*, *116*, D04108, doi:10.1029/2010JD014847.

1. Introduction

[2] Since the launch of the Television Infrared Observation Satellite (TIROS-N) in 1978, more than 30 years of observations have been made by the High-Resolution Infrared Radiation Sounder (HIRS) on board the operational National Oceanic and Atmospheric Administration (NOAA) polar orbiting satellite series (hereafter abbreviated as N#, where # is the satellite number) and the meteorological operational satellite program (Metop). There are twenty channels in the HIRS instrument, in which channel 12 observes the upper tropospheric water vapor (UTWV). Figure 1 displays the spectral response functions of HIRS channel 12 for the satellites examined in this study. The approximate spectral ranges for the HIRS/2 series and the HIRS/3 and HIRS/4 series are marked at the top of Figure 1. As a reference, the atmospheric transmittance for a typical tropical clear-sky atmosphere is also included.

[3] Studies have shown that UTWV variations are closely associated with large-scale circulation changes, particularly with the El Niño–Southern Oscillation (ENSO) [*Bates et al.*, 2001; *McCarthy and Toumi*, 2004; *Bony et al.*, 2006]. *Bates and Jackson*'s [2001] study showed the variation of derived upper tropospheric humidity in relation with the strong interactions between tropical and midlatitude planetary waves. Studies of upper tropospheric humidity derived from satellite microwave sounding data also demonstrated the association of its variability with regional systems such as the Indian summer monsoon [*Xavier et al.*, 2010].

[4] There have been more than a dozen satellites carrying the HIRS instruments in the NOAA polar orbiting satellite series. A review of the NOAA polar satellites with a focus on sounder instruments can be found in work by *Reale et al.* [2008]. Because of the independence in the calibration based on the individual HIRS instrument's channel spectral response function along with other factors, biases exist from satellite to satellite [*Shi et al.*, 2008]. Figure 2 shows the monthly mean time series of HIRS clear-sky UTWV (brightness temperatures of HIRS channel 12) from each individual satellite between 30°N and 30°S. On a monthly basis, the upper tropospheric measurements from different overlapping satellites should reflect similar values. However, consistent biases are evident among successive satellites with the same instruments. For example, the averaged difference between N11 and N12 is −1.2 K. When the HIRS instrument switched from HIRS/2 to HIRS/3, the difference between N14 and N15 is about 8 K. The UTWV is a fundamental climate data record and is a key component to water vapor feedback. It is important that the intersatellite biases are corrected.

[1]National Climatic Data Center, NOAA, Asheville, North Carolina, USA.

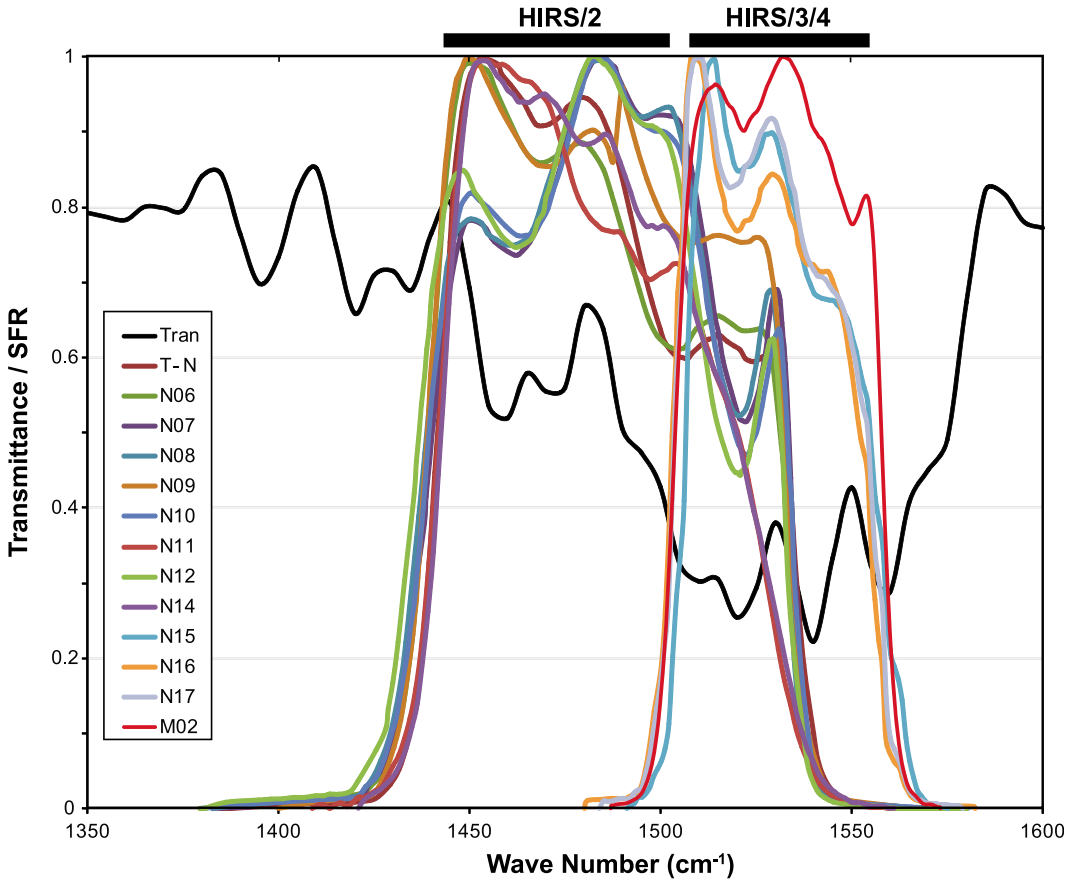

Figure 1. Spectral response functions of HIRS channel 12. As a reference, the atmospheric transmittance for a typical tropical clear-sky atmosphere is included (black line). The approximate spectral ranges for the HIRS/2 series and the HIRS/3 and HIRS/4 series are marked at the top.

[5] Considerable effort was made by *Bates et al.* [1996] to adjust the HIRS intersatellite biases. An empirical method was applied to intercalibrate 13 years (1981–1993) of HIRS data. In the analysis, the data were binned on 2.5° by 2.5° grids for 5 day averaged (pentad) data. A 13 year mean for each location based on each pentad and each satellite was calculated. The anomaly relative to this mean was then computed for the data set for each satellite. The anomalies were compared between two satellites for the same target assuming that the statistical distributions of anomalies were the same. On the basis of the comparison, the satellites were adjusted to N07 as a base satellite to produce a self-consistent data set of global observations. This intersatellite calibrated data set facilitated numerous studies on the variability and trend of upper tropospheric humidity [*Geer et al.*, 1999; *Bates and Jackson*, 2001; *Bates et al.*, 2001; *McCarthy and Toumi*, 2004], evaluation of climate model simulations [*Iacono et al.*, 2003], and examination of upper tropospheric moistening

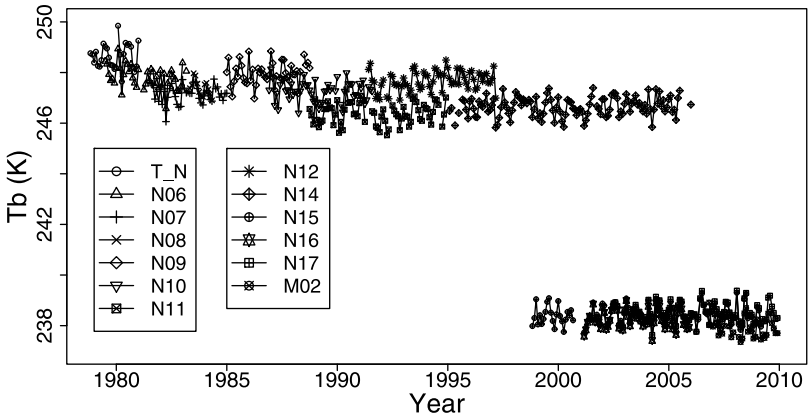

Figure 2. Monthly mean time series of HIRS UTWV brightness temperatures from each individual satellite, averaged from 30°S–30°N latitudes.

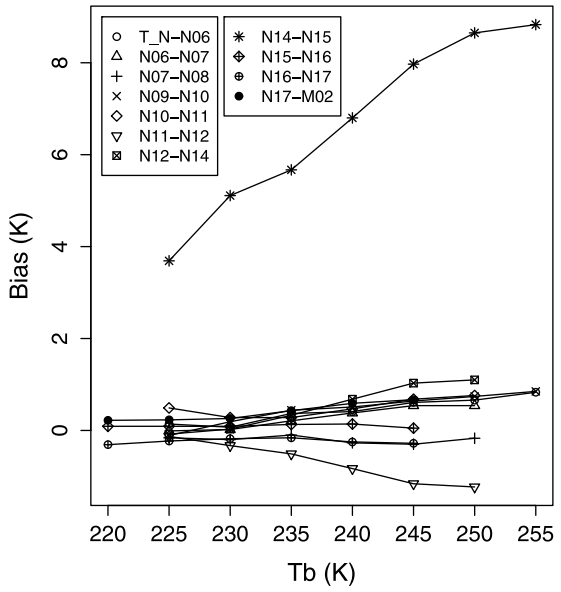

Figure 3. Sequential intersatellite biases of UTWV brightness temperatures for 11 pairs of satellites as functions of the brightness temperature.

[*Soden et al.*, 2005]. However, the intersatellite calibration method carried out by *Bates et al.* [1996] is based on HIRS/2. With the change of HIRS instrument to the HIRS/3 design on the NOAA KLM series starting in 1998 and HIRS/4 design on the Initial Joint Polar-Orbiting Operational Satellite System satellites series (N18, N19, METOP-A, and subsequent METOP satellites), a need to combine the newer HIRS measurements and to extend the UTWV time series to present has arisen.

2. Intersatellite Biases

[6] Recently, *Cao et al.* [2005] and *Shi et al.* [2008] used simultaneous nadir overpass (SNO) observations to intercompare radiances measured by HIRS channels. The SNO database was developed to quantify the observed radiance differences measured by HIRS on different satellites with little ambiguity. However, because the satellites intersect with each other in high latitudes, the SNO data represent only a small portion of the dynamic ranges of global data. *Cao et al.* [2009] used the Infrared Atmospheric Sounding Interferometer (IASI) observations to calculate the radiances for HIRS instruments to separate intersatellite biases induced by the spectral response functions. The examination covered the dynamic ranges of selected temperature sounding channels, however the additional factors contributing to the intersatellite biases, especially for the water vapor channels, still needed further study. In the present work a new approach is developed to derive the clear-sky HIRS intersatellite biases on the basis of matched zonal averages from the equator to the poles. We first divide the global data into 10° latitude belts centered from 85N to 85S. Monthly means of these latitude belts are computed for each satellite. For the overlapping satellites, the intersatellite differences (biases) of monthly means are obtained along with the monthly mean brightness temperature to account for the temperature-dependent features of the intersatellite biases.

[7] The intersatellite biases for Television and Infrared Observation Satellite (TIROS_N), N06 to N17, and METOP-A (labeled as M02) are shown in Figure 3. For the satellites processed, the biases are computed by subtracting the zonally matched brightness temperatures of each satellite from those of the previous satellite (for example, the bias between N16 and N17 is T_b(N16) − T_b (N17)). For every 5 K temperature bin of the HIRS observation, the associated intersatellite biases are extracted from the zonally matched data and averaged. In Figure 3, each plot represents the averaged intersatellite bias for the brightness temperatures centered at the indicated value with the range of −2.5 and +2.5 K.

[8] As expected, bias values are very large between N14 and N15. This is caused by the channel frequency change from about 1480 cm^{-1} on N14 and earlier satellites to 1530 cm^{-1} on N15 and later satellites (as shown in Figure 1). Because of the frequency change, the sensors on N14 and N15 essentially observed water vapor at different heights, which lead to the large bias of more than 8 K at the warm temperature observations. For other satellite pairs with similar channel response functions, the biases are within the range of ±1.2 K. Many satellite pairs have bias variations of more than 0.5 K across the scene temperature ranges. Small bias values are found at the low brightness temperature range. The patterns of the temperature bias variations are very similar to the bias variations of SNO measurements as shown by *Shi et al.* [2008]. Basically, the temperature-dependent biases shown in the low-temperature range of SNO are extended by the bias variation curves derived in the current study into the warm temperature range with the continued increasing or decreasing patterns. A comparison of the bias data set from current study with the SNO measurements reveals that at the observation temperature of 220 K, the differences of biases between the two data sets are within 0.2 K for almost all satellite pairs (except for N14-N15 because of large spectral change). However, the SNO measurements are limited to a much smaller temperature range over the polar regions, while the approach in the current study provides intersatellite bias data for the observations from 220 K to over 250 K.

3. Intersatellite-Calibrated UTWV Time Series

[9] The HIRS data are first processed to remove cloudy pixels for the water vapor field. The cloud clearing procedure follows the method detailed by *Jackson et al.* [2003]. The process is accomplished using a simplified method based on the ISCCP cloud detection approach [*Rossow and Garder*, 1993]. This approach combines spatial and temporal variations in the brightness temperature and applies thresholds to these variations to detect clouds. Limb correction is applied with a linear multivariate regression algorithm using multiple HIRS channels [*Jackson et al.*, 2003]. The base satellite for intersatellite calibration in the previous study of *Bates et al.* [1996] was N07. However, because there is no overlap between N08 and N09 observations, in this study we choose to use a base satellite that is within the much longer time series of N09 to Metop-A, in which there are at least two overlapping satellite observations between consecutive satellites. Among these satellites, N12 is in the middle of the 30 year time series, and the mean of the time

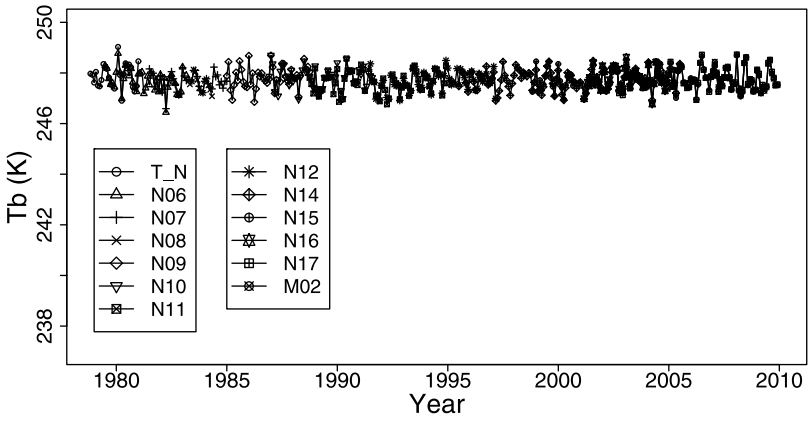

Figure 4. Intersatellite-calibrated monthly mean time series of HIRS UTWV brightness temperature from each individual satellite, averaged from 30°S–30°N latitudes.

series intercalibrated to N12 is close to the mean of the time series intercalibrated to N07, therefore N12 is chosen to be the base satellite for easy comparison with the earlier intersatellite calibration work. On the basis of the intersatellite bias data set as described in section 2, the HIRS UTWV brightness temperatures observed by individual satellites are adjusted to the values as if observed by the N12 HIRS channel. The adjustment is done to each pixel, not by moving the mean time series of a satellite to the mean time series of N12. If there is a trend in the long-term channel 12 measurement, this intersatellite calibration method is expected to retain the trend. The intersatellite biases for UTWV between N08 and N09 are estimated by comparing the time series to the one using methods developed by *Bates et al.* [1996]. An ad hoc bias value of −0.3 K is derived on the basis of the comparison. After bias adjustments are applied to each cloud-free pixel of the TIROS-N, N6 through N17 and Metop-A measurement, the pixel data are mapped to 2.5° × 2.5° latitude/longitude grids, and the gridded daily and monthly means are computed.

[10] The intersatellite calibration algorithm is designed to minimize the differences among different satellite measurements. Figure 4 shows the intersatellite calibrated monthly mean time series of UTWV brightness temperatures from TIROS-N, N06 through N17, and Metop-A (labeled as M02) from January 1979 to December 2009. General agreement is found among multiple satellites for the periods that there are overlapping satellites. The large jumps in observations from satellite to satellite as displayed in Figure 2 are removed. The data from the ATOVS satellites (N15 and after) are brought to the TOVS satellite level with similar overall variance between HIRS/2 and HIRS/3. The time series can continually be extended using this method. Comparison of this time series to the time series generated on the basis of the algorithm described by *Bates et al.* [1996] for 1979–1998 also reveals good agreement.

[11] Detailed examination of the intercalibrated time series shows that small differences remain between overlapping satellites. Many of these differences can be explained by the nature of the clear-sky data. The cloud conditions vary at different observation times of different satellites. The monthly means for different satellites are thus often the averages of different days in a month, which lead to slight differences in monthly means. To quantify the remaining intersatellite differences that have not been removed by the intercalibration algorithm, the differences of intersatellite-calibrated monthly mean HIRS UTWV brightness temperatures between the overlapping satellite pairs are shown in Figure 5. In Figure 5 each plotted value represents the average of gridded monthly mean differences from 30°S to 30°N. The difference is calculated by subtracting the later satellite

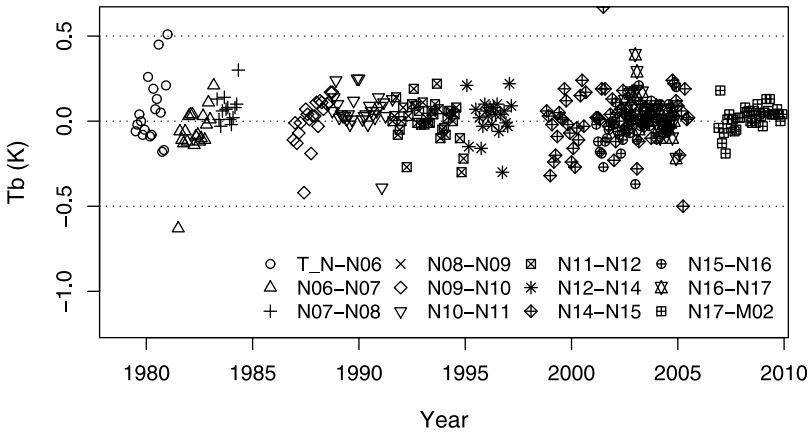

Figure 5. Differences of intersatellite-calibrated HIRS UTWV monthly mean brightness temperatures between individual satellites, averaged from 30°S–30°N latitudes.

Table 1. Averaged Remaining Differences (K) and Variances (K) of Intersatellite Calibrated HIRS UTWV Monthly Mean Brightness Temperatures Between Individual Satellites for 30°S–30°N Latitudes

	Pairs										
	T_N-N06	N06-N07	N07-N08	N09-N10	N10-N11	N11-N12	N12-N14	N14-N15	N15-N16	N16-N17	N17-M02
Average Difference	0.076	−0.065	0.073	0.008	0.059	0.006	0.020	0.005	−0.024	0.050	0.020
Variance	0.038	0.026	0.008	0.019	0.013	0.012	0.014	0.026	0.013	0.014	0.005

value from the earlier satellite value. Figure 5 displays that the monthly differences of intercalibrated time series are mostly within ±0.2 K, and almost all the monthly differences are within ±0.4 K. The averages of these remaining differences for each satellite pair during overlapping months of the full satellite time period are presented in Table 1. The list shows that the averaged differences are all near zero, and none of the averaged differences is larger than 0.1 K. It is important that the difference clusters of individual pairs of satellites are all closely grouped around 0 K. This ensures that the discontinuities among the uncorrected individual satellite series are minimized in the intercalibrated satellite series. Table 1 also lists the variance of the plots for each pair of satellites. It shows that the earliest satellites (the pair of T_N and N06 and the pair of N06 and N07) and the pair of N14 and N15 have relatively large variances of greater than 0.025 K. This indicates relatively large uncertainties in the intersatellite calibration of these satellites. For all other satellite pairs, the variances are less than 0.02 K.

[12] The climatological monthly means and variances of HIRS UTWV brightness temperatures for 30°N–30°S based on 30 years of data are shown in Figure 6. There are two peaks of mean UTWV brightness temperatures, one in winter (January) and another one in summer (June). During these two seasons the subtropics are dominated by a belt of strong subsidence (in northern hemisphere during winter and in southern hemisphere during summer) which contributes to the large values of the mean brightness temperatures. The low values of the UTWV brightness temperatures are found in April and November, indicating weaker descending branch of the general circulation during spring and fall. Large variances occur during the winter and early spring months. These are often the months associated with the El Niño events.

[13] A global UTWV monthly anomaly time series is computed on the basis of the intersatellite calibrated data. Figure 7 depicts the time-longitude section of UTWV monthly data near the equator for longitude 120E to 60W. This longitude section basically covers the equatorial Pacific region. The data shown in Figure 7 are the averages of 7.5N to 7.5S latitudes. This diagram serves two purposes. First, it is an additional check of the intersatellite calibration. Any discontinuity from satellite to satellite would show up in the diagram. Second, it tracks major tropical events such as El Niño Southern Oscillation. There were no notable jumps in

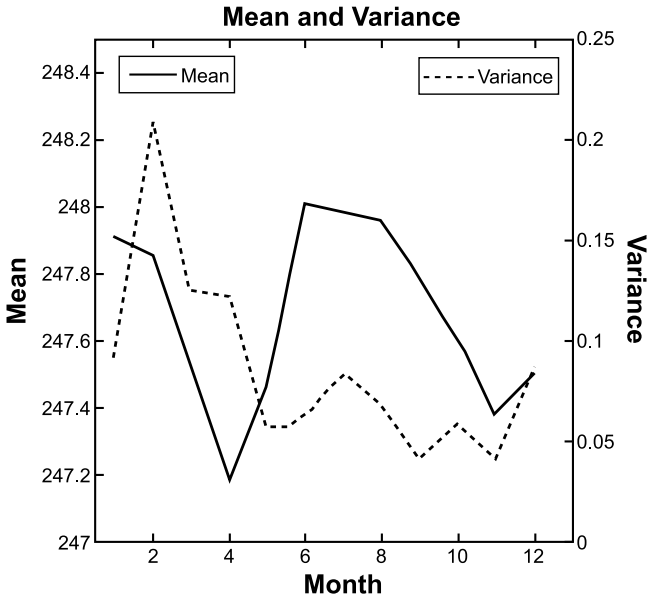

Figure 6. Climatological monthly mean and variance of HIRS UTWV brightness temperatures for 30°N–30°S, 1979–2009.

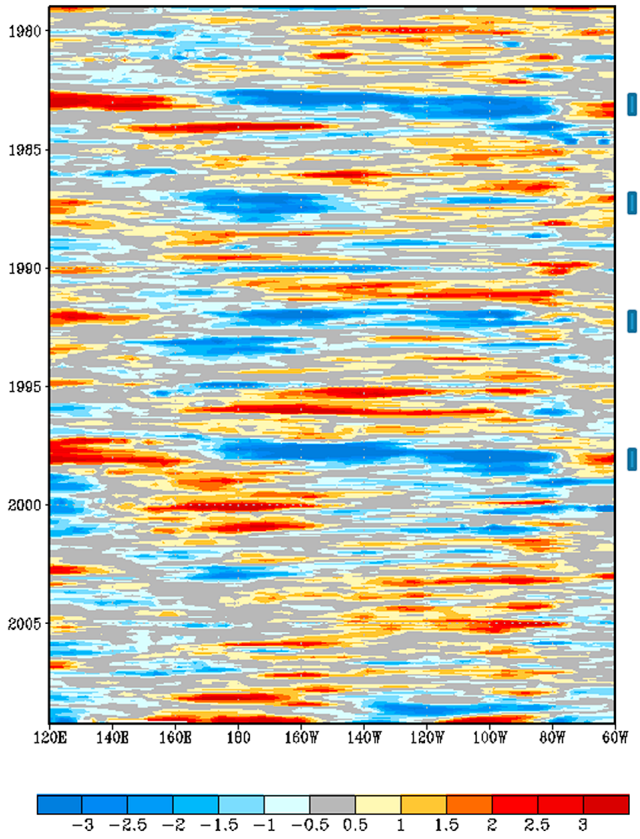

Figure 7. Time versus longitude section of HIRS UTWV brightness temperature monthly anomaly. The analysis is based on averages of data between 7.5°N and 7.5°S. The major El Niño events are marked with bars at the right side.

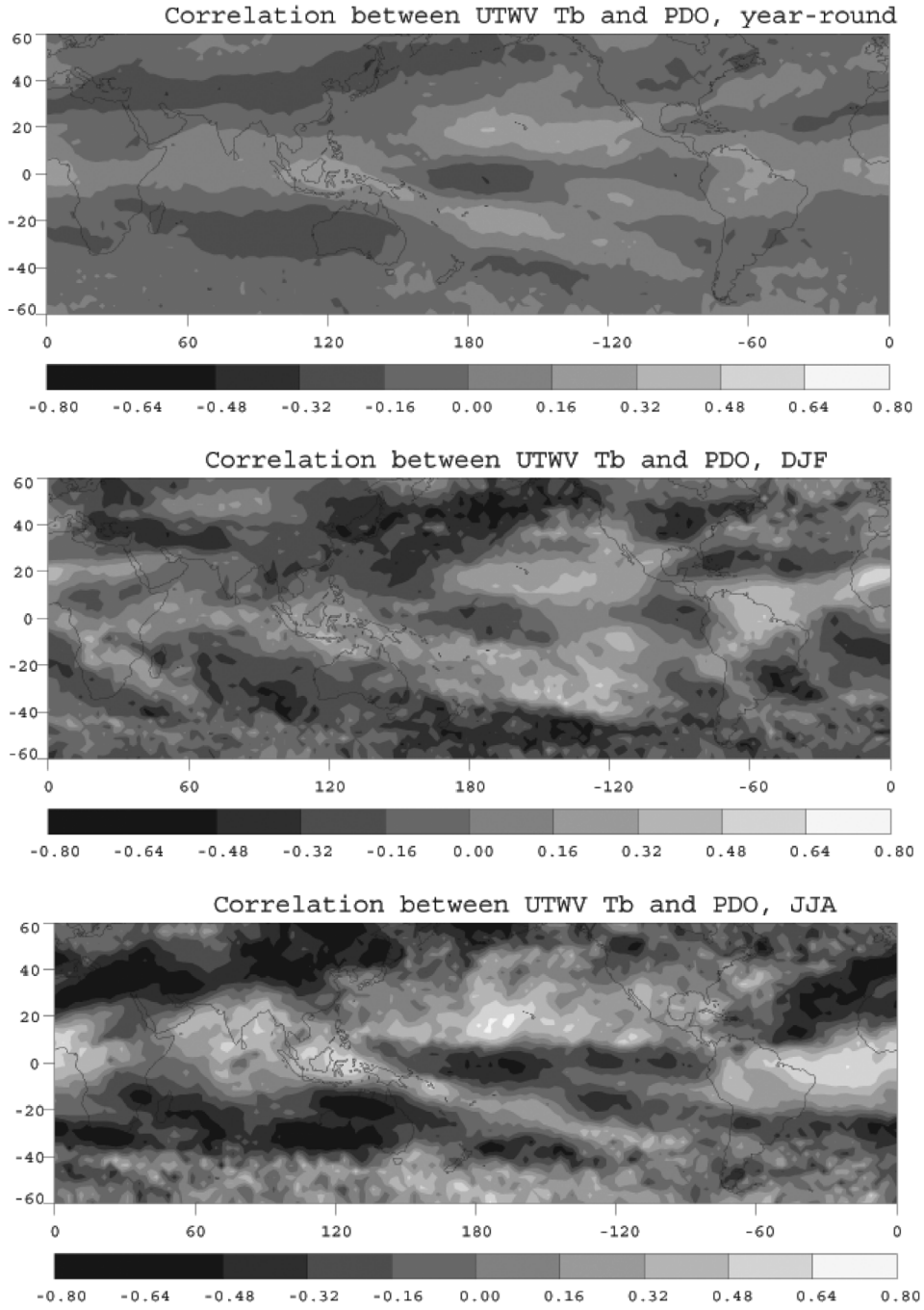

Figure 8. One-point correlation between UTWV brightness temperature and PDO index for year-round, DJF, and JJA.

observations from the beginning nor from the end of each satellite. This indicates a smooth transition of intersatellite data.

[14] Significantly lower values of UTWV brightness temperatures, which represent higher water vapor content, are observed over the equatorial Pacific before and during major El Niño events. For example, at the end of 1996 before the onset of the 1997–1998 El Niño, anomalously low UTWV brightness temperatures (marked by blue color around the dateline region) started in the western equatorial Pacific. This feature is consistent with *McPhaden*'s [1999] study which showed that higher water vapor concentration can be linked to a buildup of heat content in the atmosphere due to stronger than normal trade winds associated with a weak La Niña in 1995–1996. Through 1997, excessively high water vapor anomalies formed in the central Pacific and successively extended to the eastern Pacific. In the meantime, a dry region developed in the western Pacific. *Chandra et al.* [1998] also showed significantly increased water vapor mixing ratio at 215 hPa over the eastern Pacific in the 1997–1998 El Niño event, indicating that a deep convection layer evident in Figure 7 extended all the way to

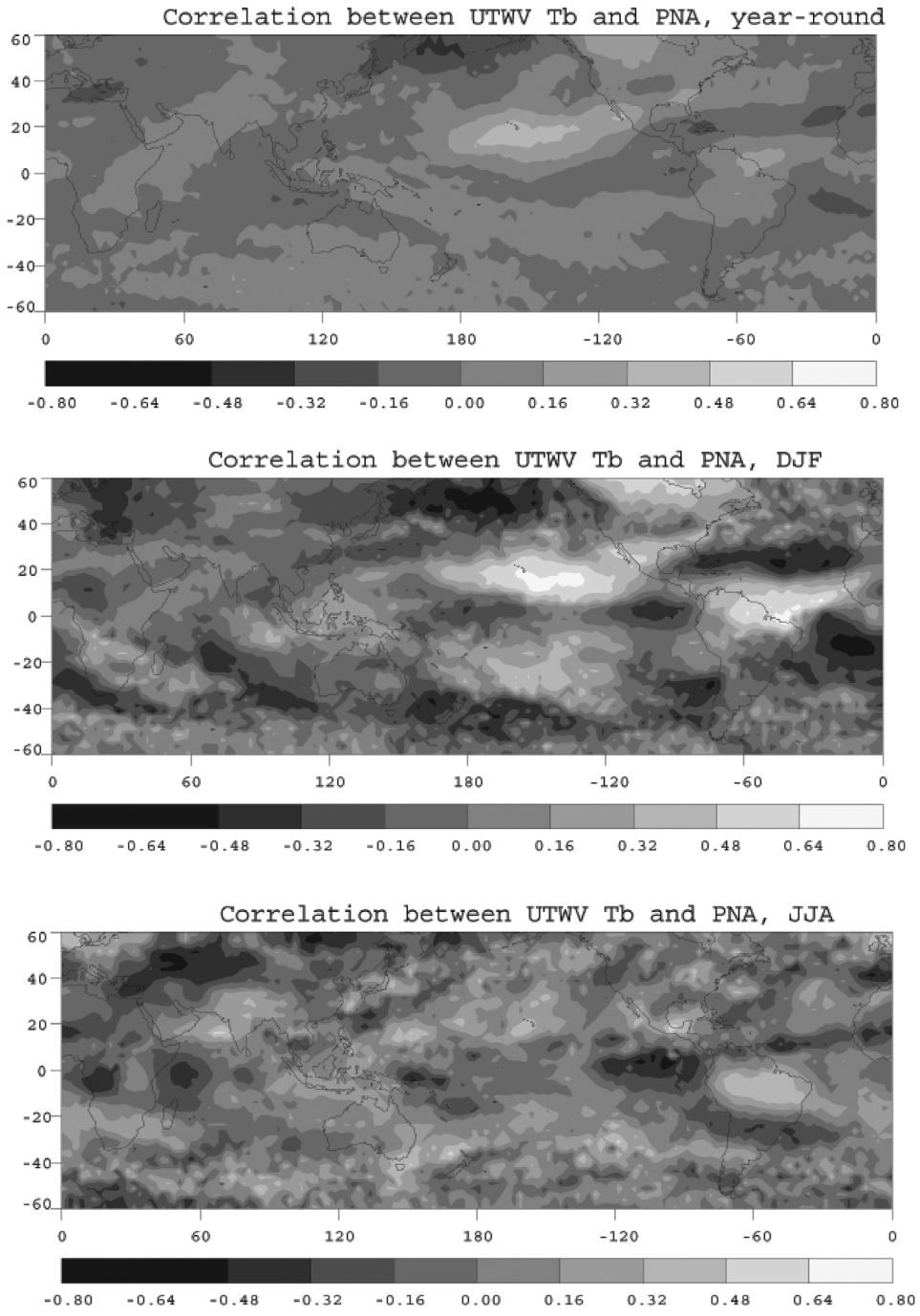

Figure 9. One-point correlation between UTWV brightness temperature and PNA index for year-round, DJF, and JJA.

the tropopause. Figure 7 also shows that the 1982–1983 El Niño evolved in a very similar pattern as the 1997–1998 event, although the patterns of other less intense El Niño events are different. Major La Niña events such as the ones in 1988–1989 and in 1998–2001 are marked by increased UTWV brightness temperature anomalies.

[15] To examine the relation of the UTWV brightness temperatures with various global events, we computed one-point (pairwise) correlation maps between the brightness temperatures and several climate indexes. The selected indexes include the Pacific Decadal Oscillation (PDO) index and the Pacific and North America (PNA) index. The results are shown in Figures 8 and 9. Figures 8 (top) and 9 (top) display the correlation map taking each of the months into account. In Figures 8 (middle and bottom) and 9 (middle and bottom), winter averages from months of December, January, and February (DJF) and summer averages from months of June, July, and August (JJA) are first calculated for both the UTWV brightness temperatures at each grid and the index data. The one-point correlations between the

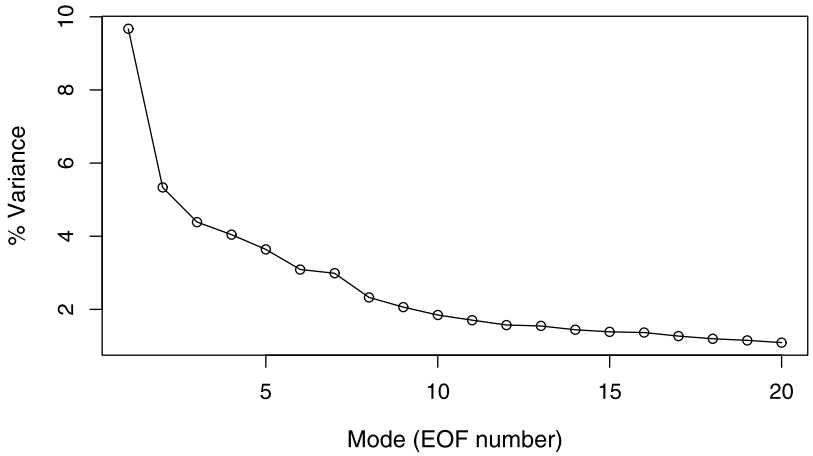

Figure 10. Percent variances of the first 20 EOF modes for UTH.

brightness temperatures at each grid and the index data are then computed.

[16] The PDO index is based on the North Pacific sea surface temperature anomalies poleward of 20°N. The index has a tendency for multiyear and multidecadal persistence. The PDO events (mostly positive index values) have persisted for 20–30 years since the late 1970s. The climatic fingerprints of the index are most visible in the North Pacific and North America, with secondary signatures in the tropics [*Mantua and Hare*, 2002]. Numerous studies found that PDO is closely associated with ENSO and other forcings [e.g., *Newman et al.*, 2003; *Schneider and Cornuelle*, 2005], though the time scales of the forcings are different. In Figure 8, relatively large negative correlations (reflecting positive correlation between higher water vapor and PDO index) are found in DJF over the subtropics of the northwestern Pacific Ocean, the Asian continent, and North America, while positive correlations are found in tropical eastern Pacific Ocean and South America. In JJA the correlations over the northern Pacific Ocean, equatorial Indian Ocean, and equatorial Atlantic Ocean are positive, while negative correlations stretch from Asia to Africa in 20–40N and in North Atlantic Ocean. Throughout the year, a positive correlation region is located in the eastern Pacific Ocean between the equator and 20°N, and a continuous negative correlation belt extends from subtropical North Pacific Ocean, passing through the Asia, and into northern Africa and ending in eastern Atlantic Ocean.

[17] The PNA is one of the prominent modes of low-frequency variability in the northern extratropics. The procedure to calculate the index is described by *Barnston and Livezey* [1987] and used by *van den Dool et al.* [2000] and *Chen and van den Dool* [2003]. In the positive phase of the PNA there is a region of above-average geopotential heights of 500 hPa and 700 hPa in northern Canada with extension to northwestern United States and a region around Hawaii. Below-average geopotential heights are located in middle to high latitudes of North Pacific Ocean and in the southeastern United States [*Wallace and Gutzler*, 1981]. Figure 9 shows that the largest correlation between UTWV and PNA occurs in the winter months. Figure 9 (middle) depicts a pattern of positive correlation regions over central and eastern North Pacific and over Canada, and with negative correlation regions over northern North Pacific and along 20°N (±10°) in the Atlantic Ocean from Cuba to the coast of Africa. These features are very similar to a positive phase of PNA, especially the dipole features in northern and lower latitude of the North Pacific. However, the large positive correlation region over Canada and the negative region over Cuba extend to much larger areas to the east, compared to a typical PNA positive phase in which positive and negative anomalies are centered in western Canada and southeastern United States. This reflects a larger area of water vapor field in upper troposphere over 20°N–30°N of Atlantic Ocean corresponding to the PNA feature in midtroposphere. Other significant features in the DJF correlation map include an almost symmetric, but weaker, dipole pattern in the South Pacific, with a positive correlation region in the central South Pacific along 20°S, and a negative region along 40S. There is another positive region over northern South America elongated into 10°N of the Atlantic, associated with a negative region along 10°S–30°S of the South Atlantic. These features could be indications of teleconnection patterns in the southern Western Hemisphere. During JJA, there are weak positive correlations in the subtropical North Pacific and weak negative correlation in northern North Pacific. The correlations over Canada and Cuba are not significant. Taking all the months into account (Figure 9, top), the dipole feature in the North Pacific, with a positive region centered around Hawaii and a negative region centered near Aleutian Islands, stands out. The positive region over western Canada is evident. There is only a small area of negative correlation near Cuba.

4. Variability of Tropical Upper Tropospheric Humidity

[18] For an easier comparison of UTWV brightness temperatures with other conventional observations, *Soden and Bretherton* [1993] derived a formula to calculate the upper tropospheric humidity (UTH) on the basis of UTWV brightness temperature as

$$\mathrm{UTH} = \cos\theta e^{(31.5-0.115\,T_b)} \tag{1}$$

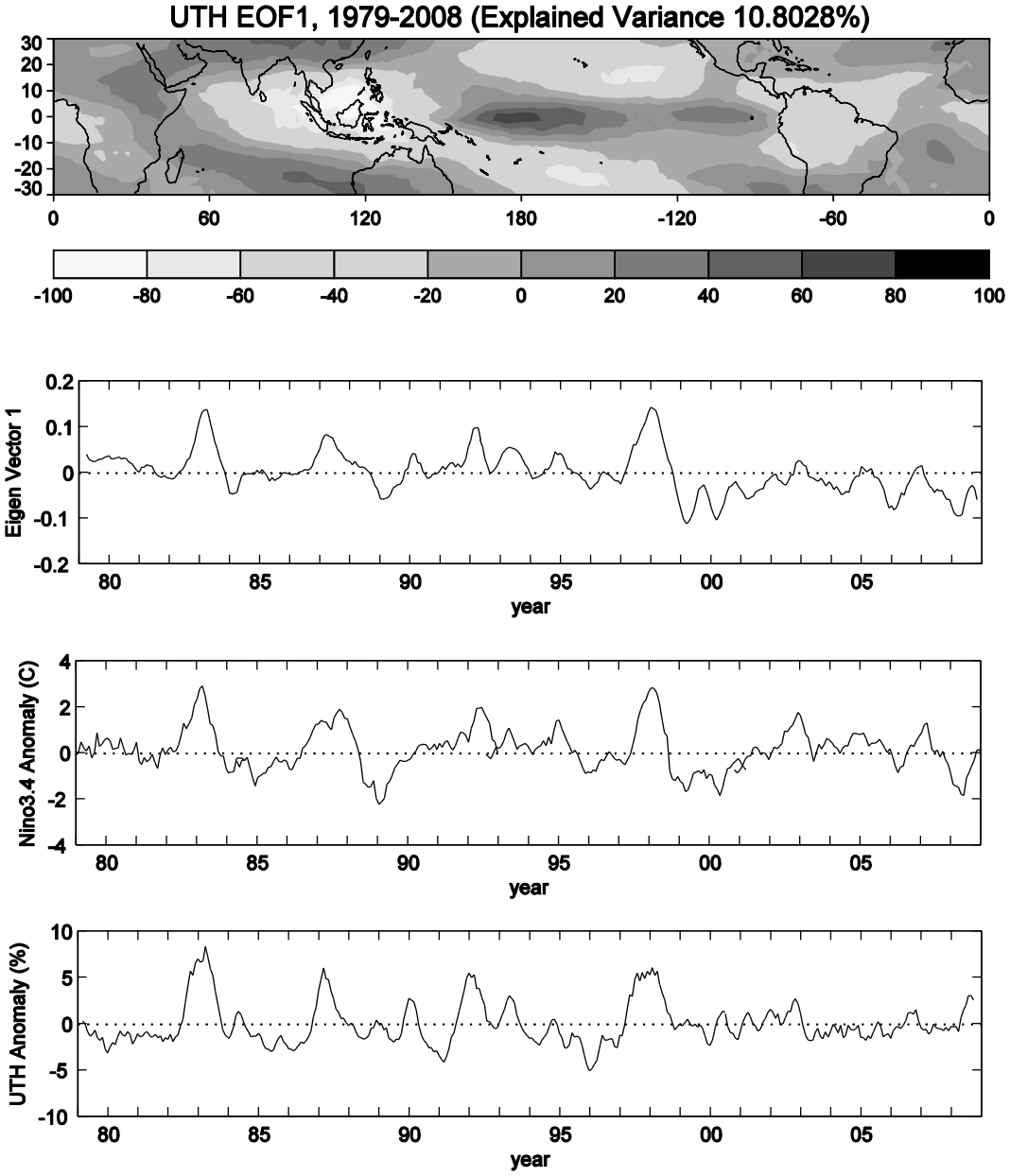

Figure 11. Leading EOF for UTH anomalies and time series for the eigenvector 1 of UTH for 30°N–30°S, Niño 3.4 SST anomaly, and UTH anomalies over the Niño 3.4 region. Five month moving average is applied to the UTH eigenvector time series and the UTH anomaly time series plots.

in which T_b is the brightness temperature of HIRS channel 12 and θ is the satellite zenith angle. This approach has been applied in several studies [e.g., *Soden and Bretherton*, 1994; *Brogniez et al.*, 2005].

[19] In the studies of *Soden and Fu* [1995] and *Soden and Bretherton* [1996] the authors used a more precise equation, in which a variable, p_0, is included as a denominator to the right side of equation (1). The p_0 denotes the pressure of the 240 K isotherm divided by 300 hPa. A modified approach was also introduced by *Jackson and Bates* [2001] to calculate UTH by incorporating a lower atmosphere temperature channel (channel 6). Both approaches require other data sets (temperature profiles or another channel) in addition to HIRS channel 12. For the simplicity of qualitative discussion based on independent data from HIRS channel 12 without relying on any ancillary data, we calculated UTH using the *Soden and Bretherton* [1993] approach. The impact of using the simplified form on the resulting UTH patterns in the tropics is not significant because the horizontal temperature gradient in the tropical upper troposphere is small. However, the simplified form tends to overestimate UTH over higher latitudes. With this in mind, we will limit our UTH discussion to the tropics.

[20] To investigate the major spatial patterns and significant events in the 30 year time series, the empirical orthogonal function (EOF) analysis is performed on the monthly 2.5° × 2.5° gridded UTH data. Figure 10 shows the percent variances contained in each of the first twenty modes. The contributions from the first five modes are 10.80%, 5.25%,

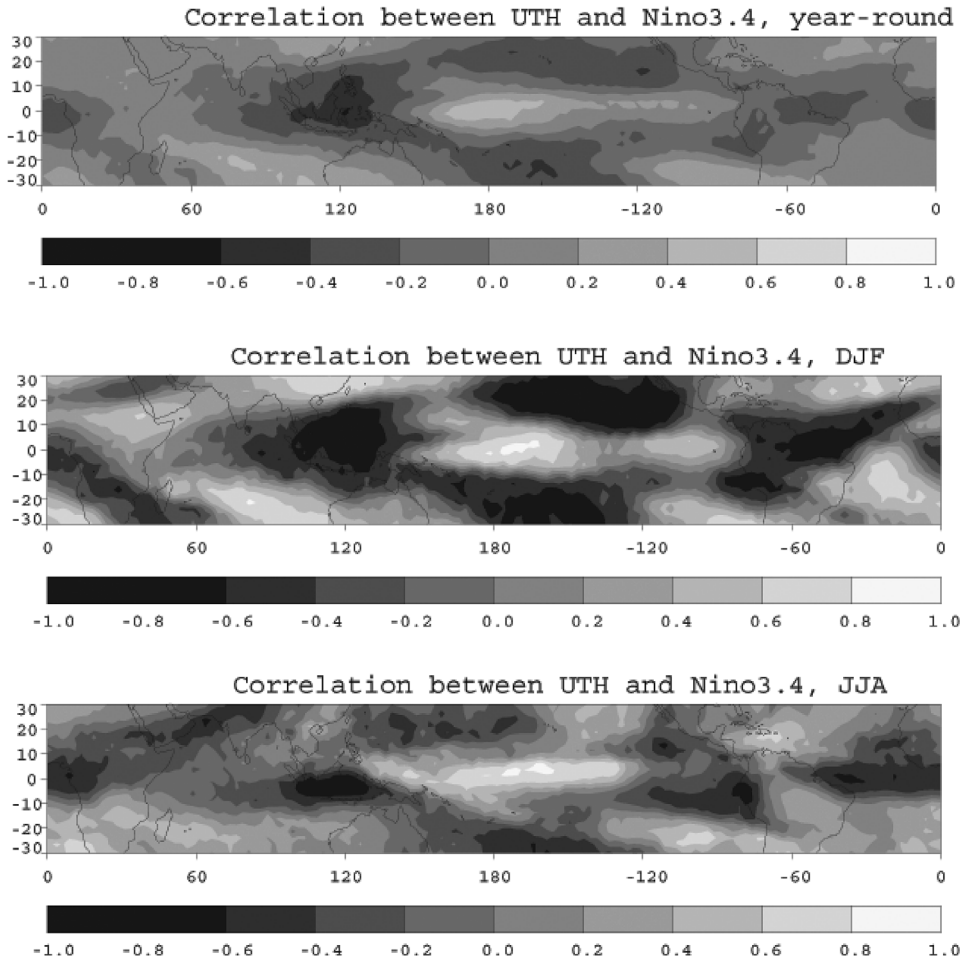

Figure 12. One-point correlation between UTH and NIÑO 3.4 SST anomaly for year-round, DJF, and JJA.

3.48%, 3.25% and 3.22%. The contribution from each of the other individual modes is less than 3%. The spatial pattern and time series of EOF mode 1 are displayed in Figure 11. For comparison, the time series of sea surface temperature (SST) anomalies in the central equatorial Pacific Niño 3.4 area and the time series of the UTH anomalies over the Niño 3.4 region are also plotted in Figure 11. The Niño 3.4 region is defined as 5°N–5°S and 170°W–120°W. In Figure 11 (top) the spatial pattern shows a belt of positive UTH over equatorial Pacific Ocean, a center of negative UTH over Indonesia with extension to the equatorial eastern Indian Ocean, and a region of negative UTH over equatorial South America. To the northern subtropic 20°N–30°N, there is a negative UTH region over the central Pacific and a positive region over the Asia continent and extending to the Africa continent. There is also a negative UTH region in the southern subtropic Pacific Ocean 20°S–30°S. A positive region is found over the southern Indian Ocean and western Australia. The corresponding time series of leading eigenvector of UTH shows that the strongest signals are found during the major El Niño events of 1982–1983 and 1997–1998. Large signals are also seen in other El Niño events such as 1987–1988 and 1991–1992. Large signals of opposite sign are evident for the La Niña events of 1984–1985, 1988–1989, 1998–2001, and 2007–2008. Comparing the time series of the leading eigenvector of UTH to the time series of Niño 3.4 SST anomaly, the features are in remarkable agreement. This indicates that the leading variability of UTH is largely dominated by the ENSO events. Figure 11 (bottom) displays the time series of UTH anomaly averaged over the Niño 3.4 region. This time series is very consistent with the Niño 3.4 SST anomaly time series. During major El Niño events the deep convection transports significant amount of moisture into upper troposphere, forming lasting humidity peaks over the warmed Niño 3.4 region.

[21] To objectively locate the areas that have largest association with the Niño 3.4 SST, we computed one-point (pairwise) correlation between the time series of UTH at each grid point and the time series of Niño 3.4 SST anomaly time series. Figure 12 (top) shows that when data throughout the year are incorporated, the largest positive correlation is found over central equatorial Pacific, and the largest negative correlation is found over western Pacific around the Indonesia region. In the subtropics, there are two belts of negative correlation, one in 20°N–30°N and another in 20°S–30°S, over the Pacific Ocean. Positive correlations are found in 20°S–30°S of the Indian Ocean, 20°S–30°S of the eastern Pacific Ocean and South America, and 20°N–30°N of the Asian continent. This map reveals that throughout the year when Niño 3.4 SST increases, the ascending branch of

Table 2. Linear Trends in HIRS UTH From Monthly Mean Data of 1979–2009[a]

Latitude Zone	Trend (%/yr)	SD (%)	Lag-1	Years Significant
30°N–20°N	−0.0205	0.031	0.132	128.8
30°S–20°S	−0.0188	0.028	0.122	68.4
30°N–30°S	0.0052	0.033	0.165	121.3
10°N–10°S	0.0254	0.038	0.231	124.1

[a]The standard deviation (SD) of the linear fit, lag-1 autocorrelation, and number of years required for the trend to achieve a 95% confidence level are also listed.

the general circulation over central and eastern equatorial Pacific Ocean strengthens and transports moisture into the upper troposphere. In the mean time the descending branches in the western Pacific and in both the northern and the southern subtropical Pacific dry the upper troposphere in these regions. The changes in atmospheric circulation related to teleconnections also enhance the convective activity over the subtropics of the southern Indian Ocean. Figure 12 (middle) shows the correlation for DJF. The correlation pattern is similar to Figure 12 (top), but with much stronger correlations. The positive correlation in the eastern equatorial Pacific Ocean is better defined. The JJA correlation map is shown in Figure 12 (bottom). During JJA, there is negative correlation in eastern equatorial Pacific Ocean, in contrast to the positive correlation in DJF. The positive correlation extending from central Africa to Asia in DJF is also replaced by negative correlation in JJA, likely due to changes in monsoon circulations.

[22] A table listing zonal long-term linear trends of UTH over the tropical region for 1979 to 2009 is displayed in Table 2. Table 2 also lists statistics including the standard deviation of the linear fit, lag-1 autocorrelation, and number of years required for the trend to achieve a 95% confidence level, computed on the basis of the analysis described by *Weatherhead et al.* [1998]. Table 2 shows that there is a slight increase of humidity between 30°N and 30°S. This is consistent with the *Bates and Jackson* [2001] HIRS data analysis of a shorter time series and in agreement with *Soden et al.*'s [2005] assessment that there is moistening in the upper troposphere. Within the tropics, there is a larger increase of humidity above the equator (0.25% per decade) than the tropical average (0.05% per decade). It is interesting to note that although the humidity over the equator tends to increase, the humidity in the subtropics (between 20 and 30 latitudes, both north and south) had decreasing trend over the last 30 years. This could be an indication of an enhancement of the general circulation with more convective activity in the deep tropics and strengthening of the descending branch in the subtropics. However, to achieve a higher level of statistical confidence, a longer times series is required as indicated in the last column of Table 2.

[23] To further investigate the UTH trends in the tropics, we analyzed the area coverage of UTH with high values (greater than 30%) and low values (less than 20%). As the data are mapped to 2.5° × 2.5° latitude and longitude grids, the number of grids is used to represent the area coverage. Figure 13 plots the time series of the numbers of grids with UTH values greater than 30% (Figure 13, top) and less than 20% (Figure 13, bottom) in 30°N to 30°S. Large seasonal variations of area coverage of both high and low values of UTH are evident in the plots. There are usually two peaks of large area coverages in a year, one in summer and another one in winter. The peaks with respect to area of large UTH values and small UTH values usually occur in the same month, indicating that when there is large organized convection in some parts of the tropics, there are enhanced descending areas in other parts of the tropics. Trend analysis on the area coverage is also performed and the results are listed in Table 3. Consistent with the tropical humidity increase as shown in Table 2, Table 3 shows that there is an increase in area of 2.9 grids/yr that has UTH values greater the 30%. On the other end, there is also an increase in area of 2.2 grids/yr where UTH has values less than 20%. The long-term increases in the area of both high and low UTH values further reveal the likelihood of enhanced convective activity in the tropics. These results are consistent with *Sohn and Park* [2010] study which showed intensified strength of both north-south and east-west tropical circulations since

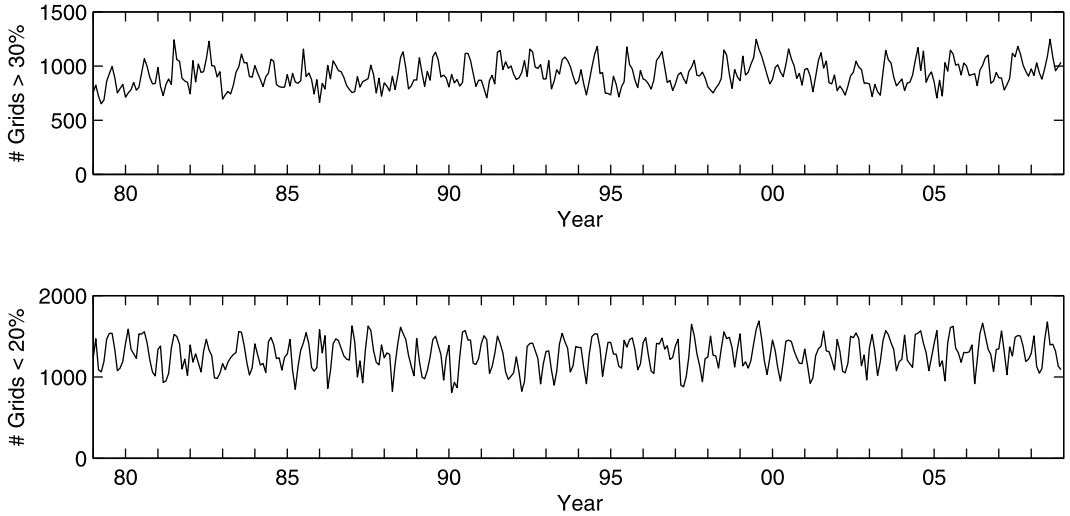

Figure 13. Time series for numbers of grids having (top) UTH values greater than 30% and (bottom) UTH values less than 20% for 2.5° × 2.5° grids in 30°N–30°S.

Table 3. Linear Trends for the Change in Number of 2.5° × 2.5° Grids for HIRS UTH Having Values Greater Than 30% and Less than 20% Over 30°N–30°S[a]

UTH Values	Trend (grids/yr)	SD (grids)	Lag-1	Years Significant
Greater than 30%	2.8701	0.644	0.248	24.5
Less than 20%	2.1989	0.787	0.139	33.5

[a]The standard deviation (SD) of the linear fit, lag-1 autocorrelation, and number of years required for the trend to achieve a 95% confidence level are also listed.

1979 on the basis of NCEP reanalysis and satellite data from the Special Sensor Microwave Imager (SSM/I) derived products and HIRS observation.

5. Summary and Discussion

[24] Intersatellite calibration is carried out for clear-sky HIRS UTWV brightness temperatures from TIROS-N to Metop-A, and a time series of over 3 decades is generated. The intersatellite calibration is done on the basis of a scene temperature–dependent scheme. The intersatellite biases are derived from time matched zonal averages from the equator to the poles. There are significant variations of bias values across the observed temperature range. For more than half of the satellite pairs, the variations of bias values from cold to high temperatures are more than 0.5 K. In general, the biases between each pair of satellites are within ±1.2 K, except for N14-N15 in which the bias is much larger as expected because of channel frequency change. The bias for N14-N15 can be larger than 8 K for the high-temperature observations. A significant portion of the biases from satellite to satellite results from the differences in HIRS spectral response functions. Additional source of biases may include onboard blackbody calibration system, nonlinear response of the detectors to incident radiation [*Cao et al.*, 2005], and other factors. The intersatellite calibration method used in this study does not distinguish what factor the bias is from. It finds out the sum of the scene temperature–dependent biases from all contributing factors to provide an end-to-end approach.

[25] On the basis of the temperature-dependent bias data set for each pair of satellites, HIRS UTWV brightness temperatures from individual satellites are adjusted to a base satellite. A time series from November 1978 to present is formed that brings together measurements from HIRS/2, HIRS/3, and HIRS/4 instruments with minimized discontinuity. The anomaly field exhibits large temporal and spatial variability. The anomalies can provide an additional useful tool to monitor the El Niño Southern Oscillation and other tropical convective events in the aspect of water vapor variation and redistribution.

[26] The correlations between UTWV anomaly and two of the low-frequency indexes featuring North Pacific and North America are examined. Correlation maps of UTWV and PDO index show that there are very different patterns in the locations of the positive and negative values in winter and summer seasons. Throughout the year the negative correlation with PDO index is not confined to the northern North Pacific, but extends across the midlatitude Asian continent. For the correlation maps of UTWV and PDA index, the year-round pattern is similar to the positive phase of the PDA index, reflecting the association of UTWV with PDA. The correlation maps also reveal several potential teleconnection regions.

[27] For the derived UTH in the tropics, the loading pattern of the first EOF shows a very similar pattern of El Niño events. The time series of the leading eigenvector of UTH is also in remarkable agreement with the Niño 3.4 SST anomaly time series, revealing that the leading variability of UTH is dominantly forced by the ENSO events. Correlation is computed between UTH and the Niño 3.4 index for each grid point. The grid correlation maps show that central equatorial Pacific UTH is positively correlated with the Niño 3.4 index, while largest negative correlations are found over Indonesia. The correlations are larger in winter months than in summer months, and there are large differences in the correlation patterns between the two seasons.

[28] Long-term trend analyses show that there is an average increase of UTH in tropics. The increase is larger over the equator. However, a decrease of UTH is found in subtropics in both northern and southern hemispheres. In the mean time, the area coverages for UTH having both large values (greater than 30%) and small values (less than 20%) increased. This dipole-like feature as well as an overall increase of humidity in the tropics implies enhanced convective activity in the tropical region in the last 30 years.

[29] Among many applications of HIRS data, a number of studies have used HIRS water vapor data to intercalibrate geostationary satellite water vapor measurements [*Brèon et al.*, 2000; *Gunshor et al.*, 2004]. The availability of the new intersatellite calibrated HIRS water vapor data has the potential to extend the time series of intersatellite calibrated geostationary satellite data significantly. Radiosonde coverage of the tropical upper troposphere still remains insufficient, especially over the vast ocean surface. The 3 decades of HIRS measurements provide an exceptionally useful global database for observing both deep tropical convection and the large-scale circulation and for evaluating climate model simulations.

[30] **Acknowledgments.** We are grateful to Darren Jackson of Cooperative Institute for Research in Environmental Sciences, University of Colorado at Boulder for providing the HIRS cloud-clearing, limb correction, and trend analysis codes and the cloud-cleared HIRS data for 1978–2001. We would also like to thank Sharon Leduc, James Kossin, Ken Knapp, and Xuepeng Zhao for the many helpful comments on the manuscript. The PDO, PDA, and Niño 3.4 indexes are obtained from NOAA Climate Prediction Center.

References

Barnston, A. G., and R. E. Livezey (1987), Classification, seasonality and persistence of low-frequency atmospheric circulation patterns, *Mon. Weather Rev.*, *115*, 1083–1126, doi:10.1175/1520-0493(1987)115<1083:CSAPOL>2.0.CO;2.

Bates, J. J., and D. L. Jackson (2001), Trends in upper-tropospheric humidity, *Geophys. Res. Lett.*, *28*(9), 1695–1698, doi:10.1029/2000GL012544.

Bates, J. J., X. Wu, and D. L. Jackson (1996), Interannual variability of upper-troposphere water vapor band brightness temperatures, *J. Clim.*, *9*, 427–438, doi:10.1175/1520-0442(1996)009<0427:IVOUTW>2.0.CO;2.

Bates, J. J., D. L. Jackson, F.-M. Brèon, and Z. D. Bergen (2001), Variability of tropical upper tropospheric humidity 1979–1998, *J. Geophys. Res.*, *106*(D23), 32,271–32,281, doi:10.1029/2001JD000347.

Bony, S., et al. (2006), How well do we understand and evaluate climate change feedback processes?, *J. Clim.*, *19*, 3445–3482, doi:10.1175/JCLI3819.1.

Brèon, F.-M., D. L. Jackson, and J. J. Bates (2000), Calibration of the Meteosat water vapor channel using collocated NOAA/HIRS 12 measurements, *J. Geophys. Res.*, *105*(D9), 11,925–11,933, doi:10.1029/2000JD900031.

Brogniez, H., R. Roca, and L. Picon (2005), Evaluation of the distribution of subtropical free tropospheric humidity in AMIP-2 simulations using Meteosat water vapor channel data, *Geophys. Res. Lett.*, *32*, L19708, doi:10.1029/2005GL024341.

Cao, C., H. Xu, J. Sullivan, L. McMillin, P. Ciren, and Y.-T. Hou (2005), Intersatellite radiance biases for the High-Resolution Infrared Radiation Sounders (HIRS) on board NOAA-15, -16, and -17 from simultaneous nadir observations, *J. Atmos. Oceanic Technol.*, *22*, 381–395, doi:10.1175/JTECH1713.1.

Cao, C., M. Goldberg, and L. Wang (2009), Spectral bias estimation of historical HIRS using IASI observations for improved fundamental climate data records, *J. Atmos. Oceanic Technol.*, *26*, 1378–1387, doi:10.1175/2009JTECHA1235.1.

Chandra, S., J. R. Ziemke, W. Min, and W. G. Read (1998), Effects of 1997–1998 El Niño on tropospheric ozone and water vapor, *Geophys. Res. Lett.*, *25*(20), 3867–3870, doi:10.1029/98GL02695.

Chen, W. Y., and H. van den Dool (2003), Sensitivity of teleconnection patterns to the sign of their primary action center, *Mon. Weather Rev.*, *131*, 2885–2899, doi:10.1175/1520-0493(2003)131<2885:SOTPTT>2.0.CO;2.

Geer, A. J., J. E. Harries, and H. E. Brindley (1999), Spatial patterns of climate variability in upper-tropospheric water vapor radiances from satellite data and climate model simulations, *J. Clim.*, *12*, 1940–1955, doi:10.1175/1520-0442(1999)012<1940:SPOCVI>2.0.CO;2.

Gunshor, M. M., T. J. Schmit, and W. P. Menzel (2004), Intercalibration of the infrared window and water vapor channels on operational geostationary environmental satellites using a single polar-orbiting satellite, *J. Atmos. Oceanic Technol.*, *21*, 61–68, doi:10.1175/1520-0426(2004)021<0061:IOTIWA>2.0.CO;2.

Iacono, M. J., J. S. Delamere, E. J. Mlawer, and S. A. Clough (2003), Evaluation of upper tropospheric water vapor in the NCAR Community Climate Model (CCM3) using modeled and observed HIRS radiances, *J. Geophys. Res.*, *108*(D2), 4037, doi:10.1029/2002JD002539.

Jackson, D., and J. Bates (2001), Upper tropospheric humidity algorithm assessment, *J. Geophys. Res.*, *106*(D23), 32,259–32,270, doi:10.1029/2001JD000348.

Jackson, D. L., D. P. Wylie, and J. J. Bates (2003), The HIRS pathfinder radiance data set (1979–2001), paper presented at 12th Conference on Satellite Meteorology and Oceanography, Am. Meteorol. Soc., Long Beach, Calif., 10–13 Feb.

Mantua, N., and S. R. Hare (2002), The Pacific Decadal Oscillation, *J. Oceanogr.*, *58*, 35–44, doi:10.1023/A:1015820616384.

McCarthy, M. P., and R. Toumi (2004), Observed interannual variability of tropical troposphere relative humidity, *J. Clim.*, *17*, 3181–3191, doi:10.1175/1520-0442(2004)017<3181:OIVOTT>2.0.CO;2.

McPhaden, M. J. (1999), Genesis and evolution of the 1997–98 El Niño, *Science*, *283*, 950–954, doi:10.1126/science.283.5404.950.

Newman, M., G. P. Compo, and M. A. Alexander (2003), ENSO-forced variability of the Pacific Decadal Oscillation, *J. Clim.*, *16*, 3853–3857, doi:10.1175/1520-0442(2003)016<3853:EVOTPD>2.0.CO;2.

Reale, A., F. Tilley, M. Ferguson, and A. Allegrino (2008), NOAA operational sounding products for advanced TOVS, *Int. J. Remote Sens.*, *29*(16), 4615–4651, doi:10.1080/01431160802020502.

Rossow, W. B., and L. C. Garder (1993), Cloud detection using satellite measurements of infrared and visible radiances for ISCCP, *J. Clim.*, *6*, 2341–2369, doi:10.1175/1520-0442(1993)006<2341:CDUSMO>2.0.CO;2.

Schneider, N., and B. D. Cornuelle (2005), The forcing of the Pacific Decadal Oscillation, *J. Clim.*, *18*, 4355–4373, doi:10.1175/JCLI3527.1.

Shi, L., J. J. Bates, and C. Cao (2008), Scene radiance-dependent intersatellite biases of HIRS longwave channels, *J. Atmos. Oceanic Technol.*, *25*, 2219–2229, doi:10.1175/2008JTECHA1058.1.

Soden, B. J., and F. P. Bretherton (1993), Upper tropospheric humidity from the GEOS 6.7 μm channel: Method and climatology for July 1987, *J. Geophys. Res.*, *98*(D14), 16,669–16,688, doi:10.1029/93JD01283.

Soden, B. J., and F. P. Bretherton (1994), Evaluation of the water vapor distribution in GCMs using satellite observations, *J. Geophys. Res.*, *99*(D1), 1187–1210, doi:10.1029/93JD02912.

Soden, B. J., and F. P. Bretherton (1996), Interpretation of TOVS water vapor radiances in terms of layer-average relative humidities: Method and climatology for the upper, middle, and lower troposphere, *J. Geophys. Res.*, *101*(D5), 9333–9343, doi:10.1029/96JD00280.

Soden, B. J., and R. Fu (1995), A satellite analysis of deep convection, upper-tropospheric humidity, and the greenhouse effect, *J. Clim.*, *8*, 2333–2351, doi:10.1175/1520-0442(1995)008<2333:ASAODC>2.0.CO;2.

Soden, B. J., D. L. Jackson, V. Ramaswamy, M. D. Schwarzkopf, and X. Huang (2005), The radiative signature of upper tropospheric moistening, *Science*, *310*, 841–844, doi:10.1126/science.1115602.

Sohn, B. J., and S.-C. Park (2010), Strengthened tropical circulations in past three decades inferred from water vapor transport, *J. Geophys. Res.*, *115*, D15112, doi:10.1029/2009JD013713.

van den Dool, H. M., S. Saha, and Å. Johansson (2000), Empirical orthogonal teleconnections, *J. Clim.*, *13*, 1421–1435, doi:10.1175/1520-0442(2000)013<1421:EOT>2.0.CO;2.

Wallace, J. M., and D. S. Gutzler (1981), Teleconnections in the geopotential height field during the Northern Hemisphere winter, *Mon. Weather Rev.*, *109*, 784–812, doi:10.1175/1520-0493(1981)109<0784:TITGHF>2.0.CO;2.

Weatherhead, E. C., et al. (1998), Factors affecting the detection of trends: Statistical considerations and applications of environmental data, *J. Geophys. Res.*, *103*(D14), 17,149–17,161, doi:10.1029/98JD00995.

Xavier, P. K., V. O. John, S. A. Buehler, R. S. Ajayamohan, and S. Sijikumar (2010), Variability of Indian summer monsoon in a new upper tropospheric humidity data set, *Geophys. Res. Lett.*, *37*, L05705, doi:10.1029/2009GL041861.

J. J. Bates and L. Shi, National Climatic Data Center, NOAA, Asheville, NC 28801, USA. (lei.shi@noaa.gov)